Earth and Space Science

RESEARCH ARTICLE
10.1029/2018EA000527

Interpretation of the Tropospheric Gradients Estimated With GPS During Hurricane Harvey

Victoria Graffigna[1,2], **Manuel Hernández-Pajares**[3], **Mauricio Gende**[1,2], **Francisco Azpilicueta**[1,2], **and Pablo Antico**[1,2]

[1]Facultad de Ciencias Astronómicas y Geofísicas Department, Universidad Nacional de La Plata, La Plata, Argentina, [2]Consejo Nacional de Investigaciones Científicas y Técnicas (Conicet), Argentina, [3]Department of Mathematics, Universitat Politècnica de Catalunya (UPC), Barcelona, Spain

Key Points:
- Major hurricane over dense GPS network gives unique opportunity to study ZTD gradients
- The ZTD gradients show changes in orientation and magnitude when synoptic front approaches

Correspondence to:
V. Graffigna,
vgraffigna@fcaglp.unlp.edu.ar

Citation:
Graffigna, V., Hernández-Pajares, M., Gende, M. A., Azpilicueta, F. J., & Antico, P. L. (2019). Interpretation of the tropospheric gradients estimated with GPS during Hurricane Harvey. *Earth and Space Science*, *6*, 1348–1365. https://doi.org/10.1029/2018EA000527

Received 31 DEC 2018
Accepted 2 JUL 2019
Accepted article online 8 JUL 2019
Published online 7 AUG 2019

Abstract During the last decade Global Positioning System (GPS) Continuous Operating Reference Stations networks have become a new important data source for meteorology. This has dramatically improved the ability to remotely sense the atmosphere under the influence of severe mesoscale and synoptic systems. The zenith tropospheric delay (*ZTD*) is one of the atmospheric variables continuously observed, and its horizontal variations, the horizontal tropospheric gradients, are routinely computed nowadays within the dual-frequency GPS processing, but their interpretation and relationship with the weather is still an open question. The purpose of this paper is to contribute in this direction by studying the effect that Hurricane Harvey had on the spatial and temporal behavior of the *ZTDs* and gradients, when it reached Texas coast, during 18–31 August 2017. The results show that *ZTD* time series present a clear and rapid increase larger than 10 cm in a few hours when the hurricane reached the area. Gradients behaviors show that the hurricane also produced significant changes on them, since the magnitude and predominant directions before and after the hurricane arrived are completely different. Noticeably, the gradient vectors before the landing are consistently related to the horizontal winds and pressure fields. In this manuscript we demonstrate that the *ZTD* gradients can show a consistent signature under severe weather events, strongly suggesting their potential application for short-term weather forecasting.

1. Introduction and Motivation

The Global Positioning System (GPS) was initiated in the 1970s, became fully operational in 1994, and rapidly showed its potential as a resource for high-precision (millimeter-level) geodetic measurement, apart from its wide use in navigation. The need to precisely estimate the error sources on the GPS signal to improve the positioning gave place to a new application of GPS, the remote sensing of atmospheric water vapor (Bevis et al., 1992). GPS meteorology is able to provide atmospheric variables with high spatiotemporal resolution at no further cost. Nowadays, this new area is a well-established field in both research and operation (Guerova et al., 2016) for some large regions in the world and has become an important source of climate monitoring. However, as a consequence of the significant improvements in GPS processing algorithms, inconsistencies in long-term time series have been introduced; therefore, there is a need for a homogeneous set of data for GPS meteorology. In this sense, the GPS community has contributed with reprocessed data that are useful for many applications (Dousa et al., 2017; Pacione & Di Tomaso, 2016).

The zenith tropospheric delay (*ZTD*) is indeed one of the parameters estimated in the GPS data processing, and it represents the vertically integrated atmospheric refractivity, which is a function of pressure, temperature, and water vapor content (Davis et al., 1985). The slant (*STD*) is modeled as the *ZTD* plus its horizontal gradients, because the *ZTD* is common to all the lines of sight for a given GPS receiver at a given time and therefore computed for all the satellites as only one unknown. Moreover, studying and understanding the azimuthal distribution of the tropospheric delay increases the ability of sensing the atmosphere with GPS (Elgered et al., 2018).

The densification of the GPS networks like Continuous Operating Reference Stations (CORS) in North America, Europe (EUREF Reference Frame Sub-Commission for Europe Permanent Network - EPN; Bruyninx et al., 2012), Japan (GeoNet; Sagiya, 2004) and South America (SIRGAS-CON; Brunini, 2007), have strengthened the application of the tropospheric gradients on the study of mesoscale distribution of

atmospheric variables, typically not well monitored (Boniface et al., 2009). Several projects have been pursued to study this subject, starting as early as in the 1990s (GPS/MET from UCAR in 1993) until now [ESSEM COST Action ES1206/GNSS4SWEC or E-GVAP [the EUMETNET EIG Global Navigation Satellite Systems (GNSS) water vapor programme] dealing with the usage of ground-based GPS delay in operational meteorology) . Zhang et al. (2015) have found that thanks to the dense GPS networks, Victorian CORS in this case in Australia, it was possible to follow a synoptic signature of the dynamics of the event and offer precursors to severe weather with tropospheric parameters derived from GPS observations.

On a global scale, the tropospheric gradient vector appears pointing toward the equator, and annual and semiannual frequencies are usually detected on long time series (Meindl et al., 2004). However, this behavior can change locally and when strong convection takes place or when the topography appears rugged (Karabatić et al., 2011; Shoji, 2013; Shoji et al., 2004). An important question that is still open and that several recent works have tried to answer is to what extent the horizontal tropospheric gradients contain real tropospheric information. Many studies have been developed and showed that horizontal gradients from ECMWF (European Centre for Medium-Range Weather Forecasts) and water vapor radiometers (WVR) do agree with GPS-estimated ones at the level of 0.5 mm for ECMWF and with a correlation of about 50% with WVR. See, for instance, Kačmařík et al. (2017), Dousa et al. (2017), Lu et al. (2016), Li et al. (2015), and Bar-Sever et al. (1998). Morel et al. (2015) have studied the behavior of the tropospheric gradients in Corsica island and have found that they can be influenced by both the slope of the relief and land/sea contrast in a mean year behavior. Indeed, more study on the subject is still required to understand their physical meaning. More recently, Elgered et al. (2018) have found that linear horizontal gradients derived from GPS are related to meteorological phenomena and that if any linear trend is detected, then it is likely to be related to monumentation or receiver problems.

Implementation of tropospheric gradients can be treated as a piecewise linear function or assumed constant for a significant period of time, as in GAMIT (Herring et al., 2006) from Massachusetts Institute of Technology or Bernese (Dach et al., 2015) from University of Berne. This strategy can provide n gradients per day, which can assure convergence and stability on the processing, where the resulting parameters are somehow averaged over the period. However, high-resolution gradients are needed to contribute to heavy rainfall nowcasting (Shoji, 2013), and they can be estimated with higher frequency, as an epoch-wise dependent parameter, for example, random walk (stochastic process) like in GISPY-OASIS (GNSS-Inferred Positioning System and Orbit Analysis Simulation Software package (Bar-Sever et al., 1998), from here on called GIPSY) from the Jet Propulsory Laboratory. In this work we have pursued the latest method, because we want to be able to capture sudden variations of the gradients, like prominent peaks, not necessarily linear which can be associated with synoptic fronts (Lu et al., 2016). Therefore, we have modified an in-house software to estimate horizontal gradients as an stochastic variable, adding a pair of unknowns per epoch to the system. We will show the corresponding agreement with respect to an external source that has implemented independently the same methodology.

Over the last past decade a lot of effort has been put on precise quantification of atmospheric parameters with space and ground techniques aiming to support weather forecasting (see, e.g., De Haan, 2013). The *ZTD* has played an important role on forecasting the weather, and its assimilation into weather systems is an important issue to assess (Poli et al., 2007). Many analysis centers nowadays are producing and disseminating real-time *ZTDs*, and the effort has shown to improve monitoring severe storms conditions, like for instance the Geodetic Observatory Pecný (Dousa & Vaclavovic, 2014). Karabatić et al. (2011) have shown that introducing *ZWD* to weather front analysis can forecast heavy rainfall better than only by using ground meteorological data, due to the fact that GPS derived parameters do not present a delay like those from meteorological ground stations and the improvement can be seen specially during the summer. Horizontal tropospheric gradients have become of interest for such applications, and the effective assimilation by the centers of these values into their predictions is yet an open scenario. In this sense, data assimilation algorithms are being developed in order to assess the improvement on the refractivity field by means of incorporating horizontal delay gradient in addition to *ZTD* (Zus et al., 2019). The temporal and spatial resolution of GPS observations as long as epoch-wise parameter estimation set a potential improvement on forecasting events. Hence, precise determination of gradient delays and realistic interpretation of their variability is needed before assimilating them.

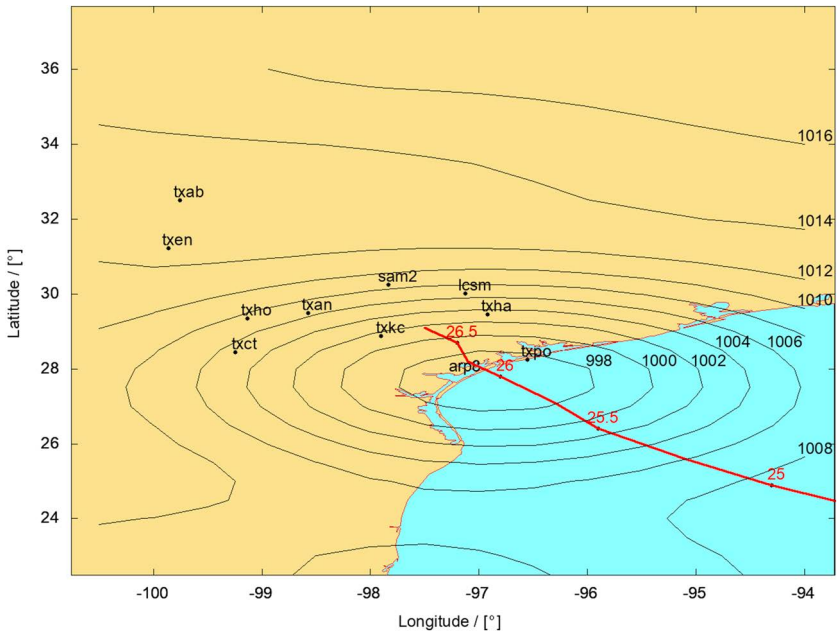

Figure 1. GPS Network selected for the study and track followed by Hurricane Harvey's eye in red. Annotated as *dd.dd* are the days of August of 2017 (UTC) of the eye's position. The isolines correspond to the moment of the landfall pressure field, and the units are in hectopascals. Note: *arp8* and *txpo* are sites located at 1-km distance but have been plotted separated for clarity of the map. txpo is on its actual location.

In this contribution we are going to assess the possible relationship that the horizontal gradients derived from GPS data processing can have with physical processes. In this case we have selected a hurricane that made landfall around 03:00 UTC on 26 August (DOY [day of year] 238) 2017, Hurricane Harvey, at peak intensity on the southern coast of United States with winds of 215 km/hr and an atmospheric pressure of 937 hPa. The isolines in Figure 1 represent the pressure field at DOY 238 at 00 hr. Harvey originated on 12 August (DOY 224) over the eastern Atlantic Ocean just west from northern Africa and traveled westward becoming a tropical storm on the 17th (DOY 229) of the same month. The system continued its motion entering the Caribbean Sea on the 18th striking land several times on different islands and the Gulf of Mexico later on the 23rd (DOY 235) with a significant low surface pressure.

This hurricane became the first major one to make landfall in the United States since Wilma in 2005 and, as it is known, GPS receivers are mostly located on ground and very few ones are found offshore; therefore, monitoring this type of storms with this method is unlikely, due to rapid weakening of its intensity when touching land. CORS network is located and densified in the area where Harvey mostly occasioned disaster, and its permanent receivers have already been used to study this event. Milliner et al. (2018) have been able to use this feature to track how much of the water it brought was absorbed by the ground and how much it drained rapidly to the sea, finding that that a third of Harvey's total stormwater was captured on land, indicating that the rest drained rapidly into the ocean, with the remaining stored water gradually lost over the following 5 weeks.

We have selected 11 GPS receivers from CORS network, chosen to capture the behavior of the landfall of the hurricane. Considering the track showed in Figure 1, plotted in red numbers denoting the day of August of the eye's position, we have selected sites on one and other side of the path the storm followed on ground. The 11 sites and their positions are listed in Table 1, together with detailed information about the GPS site. We have selected them rather aligned with the front, and more over the northeast region above the track of the hurricane, where the strongest intensities are to be expected. We have also added two more stations further away from the cyclone to test how they were affected.

One of the main motivations of this work is to detect and characterize early stages of a hurricane on the tropospheric gradients in order to assess if *anomalous* (not typical) patterns on the gradients are related to the state previous to the development of the low pressure center so called cyclone.

Table 1
Ellipsoidal Coordinates of the Selected Sites for the Experiments, Detailed Information About the GPS Sites, and Baseline Lengths Between Reference Station txan and Given Site

Site	Longitude (°)	Latitude (°)	Height (m)	City	GPS receiver	GPS antenna/dome	Baseline (km)
sam2	−97.83647886	30.23901344	212.801	Oak Hill	TRIMBLE NETR9	TRM57971.0/NONE	109,566988
lcsm	−97.12548843	30.00845332	74.000	Smithville	LEICA GRX1200+GNSS	LEIAR10/NONE	151,414801
txan	−98.57663350	29.49120649	265.062	San Antonio	TRIMBLE NETR9	TRM57971.00/NONE	0
txen	−99.85998169	31.21745586	608.351	Eden	TRIMBLE NETR9	TRM57971.00/NONE	228,01.690
txab	−99.75681092	32.50325278	489.758	Abilene	TRIMBLE NETR9	TRM57971.00/NONE	353,221676
txha	−96.92180618	29.45108699	63.834	Hallettsville	TRIMBLE NETR9	TRM57971.00 /NONE	160,234003
txho	−99.13444043	29.34385895	249.876	Hondo	TRIMBLE NETR9	TRM57971.00/NONE	56,450824
txct	−99.24462706	28.44208356	112.631	Cotulla	TRIMBLE NETR9	TRM57971.00 /NONE	133,516290
txkc	−97.90430947	28.87388094	111.246	Karnes City	TRIMBLE NETR9	TRM57971.00/NONE	94,707800
txpo	−97.06990232	27.83945659	−19.432	Port Aransas	TRIMBLE NETR9	TRM57971.00/NONE	235,201219
arp8	−97.05922454	27.83836206	−15.081	Aransas Pass	TRIMBLE NETR9	TRM41249USCG/SCIT	235948.629

Note. All stations are located in the United States, in the state of Texas.

This article is organized as follows. We first detail our methodology for processing the GPS data and introduce the in-house software and its validation. Then we draw a simple method for finding anomalous peaks on the horizontal tropospheric gradients time series. In section 3.1 we show the behavior of the horizontal gradients during the event. The conclusions are described in section 4.

2. GPS Processing and Validation

2.1. TOMION Software

The TOmographic Model for precise IOnospheric sounding and GNSS Navigation (TOMION) is fed with global GPS data in order to compute in real time and in postprocessing, among others, geodetic parameters, such as site coordinates, *ZTD*, global Vertical Total Electron Content maps (Roma-Dollase et al., 2017), carrier phase ambiguity fixing (Hernández-Pajares et al., 2003), etc.

The GPS computations in this research have been done based on TOMION geodetic estimation mainly developed by the second author during the last 20 years. Although the first approaches were focused on the tomography of the ionosphere, TOMION indeed acquired further features for estimating geodetic and atmosphere parameters. The background for this software on tropospheric estimations (Hernández-Pajares et al., 2001) indeed sets a potential real-time assessment of precise tropospheric gradients as well. However, back then, the strategy used was Wide Area Real-Time Kinematic (WARTK; see Hernández-Pajares et al., 2002; Hernández Pajares et al., 2010), while for this work we have used absolute positioning mode. In particular, we have applied Precise Point Positioning (PPP) as it is developed by Zumberge et al. (1997) for estimating the tropospheric parameters used for this work, and WARTK to compare and validate the new results, since the latter is extensively known.

2.2. Linear Horizontal Gradients in TOMION

The parameter estimation can be summarized as follows. The linearized *prefits* residuals ("observed minus computed") for a PPP setup, for the Iono-Free Combination can be expressed as

$$\begin{aligned}\delta P_C &= \frac{x^{sat}-x_{rec0}}{\rho^{sat}_{rec0}}\Delta x + \frac{y^{sat}-y_{rec0}}{\rho^{sat}_{rec0}}\Delta y + \frac{z^{sat}-z_{rec0}}{\rho^{sat}_{rec0}}\Delta z + c\ t_r(rec) + T^{sat}_{rec} \quad \text{and} \\ \delta L_C &= \frac{x^{sat}-x_{rec0}}{\rho^{sat}_{rec0}}\Delta x + \frac{y^{sat}-y_{rec0}}{\rho^{sat}_{rec0}}\Delta y + \frac{z^{sat}-z_{rec0}}{\rho^{sat}_{rec0}}\Delta z + c\ t_r(rec) + T^{sat}_{rec} + \lambda w^{sat}_{rec} + B_C \quad ,\end{aligned} \tag{1}$$

for the code and the phase observables, P_C and L_C respectively. In our experiments, we have taken the final coordinates of a PPP static 2-day run as a priori coordinates, computed for the sites with TOMION for the days previous to the window we are analyzing here, that is, for DOYs 229 to 230. Therefore, x_{rec0}, y_{rec0}, and z_{rec0} are the a priori coordinate for the given site and ρ^{sat}_{rec0} denotes the distance between the satellite (*sat*) and the a priori coordinate for the site (*rec*0), while x^{sat}, y^{sat}, and z^{sat} are the satellite's coordinates. In equation (1) also c is the speed of light, B_C is the Iono-Free ambiguity (integer part plus noninteger components of the

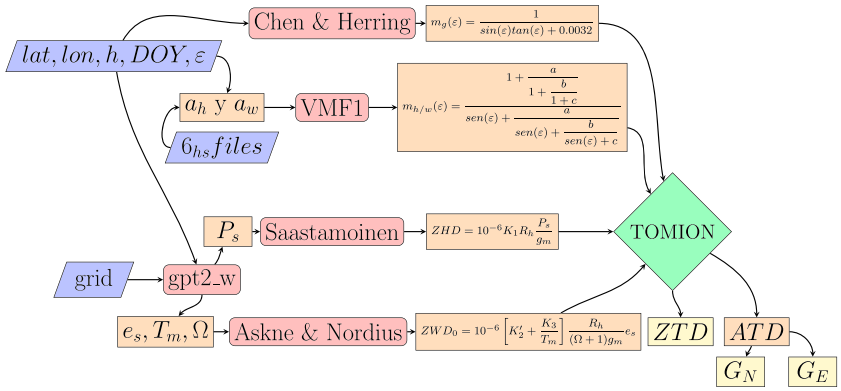

Figure 2. TOMION's implementation of tropospheric corrections. In blue are the external parameters needed for feeding the models in red. In yellow are TOMION's tropospheric estimations. a_h and a_w are the hydrostatic and wet mapping functions continued fraction form ($m_{h/w}$) coefficients, respectively. P_s is the surface pressure, e_s is the water vapor partial pressure at mean sea level, T_m is the weighted mean temperature at height H (orthometric) along the local vertical, and Ω is the water vapor decrease factor with height. The constants $K2' = K_2 - K_1(R_d/R_w)$ and K_3 are empirically determined first by Thayer (1974). R_d is the specific gas constant for the dry constituents, and R_w for the wet ones. The g_m, which is the gravity acceleration at the mass center of the vertical column of the atmosphere, can be computed as a function of the locations' latitude and H_c, which is the height of the center of mass of the vertical column of air. All the meteorological information required for the models aforementioned, including the coefficients for the mapping functions, have been taken from a model available at GGOS (2017). TOMION = TOmographic Model for precise IOnospheric sounding and GNSS Navigation ZTD = zenith tropospheric delay; ATD = asymmetrical tropospheric delay; DOY = day of year.

instrumental delays from receiver and transmitter); λ the wavelength; w is the wind-up and t_r is the receiver clock error. The terms Δx, Δy, and Δz are the corrections to the a priori values to be estimated.

The delay induced by the troposphere on GPS signals, T_{rec}^{sat} in equation (1), herein called T, can be modelled as:

$$T = m_d(\varepsilon)ZHD + m_w(\varepsilon)ZWD + m_g(\varepsilon)[G_N \cos(\alpha) + G_E \sin(\alpha)]. \quad (2)$$

according to Chen and Herring (1997). The first term in equation (2), The zenith hydrostatic delay (ZHD), has been modelled in TOMION following Saastamoinen (1972). The zenith wet delay (ZWD) has been approximately computed according to Askne and Nordius (1987). The mapping function used for this processing has been Vienna Mapping Function (VMF1; Böhm & Schuh, 2004), according to the form in Marini (1972). Detailed description of the tropospheric corrections implemented on TOMION can be seen in Figure 2.

For most applications, the first and second term in equation (2) provides enough accuracy for the user. However, for precise geodetic applications or under severe weather conditions, a third term can be considered: the asymmetrical tropospheric delay (ATD). In Figure 3 a simplification has been assumed for the sake of the approach but is valid for any direction. In this case the azimuth (α in equation (2)) is set to 90°, and

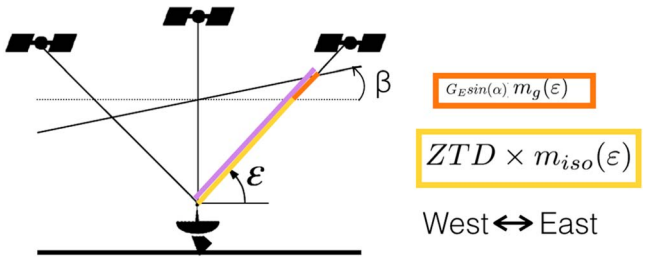

Figure 3. Scheme of asymmetric tropospheric delay, where for simplicity of the figure, east-west section is represented. In yellow is what would be accounted for if azimuthal symmetry is assumed. In orange is the correction for asymmetry. β is the tilting angle of the neutral atmosphere as defined in Meindl et al. (2004), and m_{iso} is the isotropic mapping function (VMF1). ZTD = zenith tropospheric delay.

Table 2
Processing Specifications for the Four Experiments Carried Out

Solution	Specific settings	Resolution
PPP static	Coordinates as random variables (constant)	15 min
PPP kinematic tight	Coordinates as random walk parameters 0.3 mm/$\sqrt{h}$	15 min
PPP kinematic loose	Coordinates as random walk parameters 3 mm/$\sqrt{h}$	15 min
Relative	Coordinates as random walk parameters 3 mm/$\sqrt{h}$	30 s

Note. PPP = Precise Point Positioning.

only the east gradient (G_E) is different from 0 and greater than 0. Here, the atmosphere would be "thicker" toward the east of the station and "thinner" over the west.

The *ATD* is also mapped into the zenith by:

$$m_g(\varepsilon) = \frac{1}{\sin(\varepsilon)\tan(\varepsilon) + C}, \tag{3}$$

proposed on Chen and Herring (1997). Here only the elevation angle is needed for computations and C is an empirical constant taken equal to 0.032, as suggested on the reference. In TOMION what are left as unknowns for constructing the T term are the residual *ZWD*, which means that the model on Askne and Nordius (1987) would take place as an priori value for the estimate, and G_N and G_E components, for the *ATD* term.

Then for a PPP, using the iono-free combination, for which more than 99 % of the ionospheric induced error is typically eliminated, for static antennas and P_1 and P_2 observables, our unknowns are reduced to

$$\boldsymbol{X} = [\Delta x \quad \Delta y \quad \Delta z \quad t_r \quad ZWD \quad G_N \quad G_E] \tag{4}$$

which are computed per epoch of observation, where the information a priori is available, which is 15 min for PPP and 30 s for relative.

2.3. Validation Test

In this work we have carried out four experiments. First, we have performed three different PPP processing strategies: static and kinematic, where this last one was set up for two different random walk processes for the site's coordinates, 3 and 0.3 mm/$\sqrt{\text{h}}$ approximately. We are referring to them from now on as loosely and tightly constrained, respectively. These process noise are very small and equivalent to up to 10- and 1-cm coordinate displacements over a period of 2 weeks respectively, for events similar to Harvey (see, e.g., Miyazaki et al., 2003). As it is stated in Zumberge et al. (1997), precise final orbits and satellite clocks are needed for these implementations that have been taken from the International GNSS service, with a resolution of 15 min. Thus, the spacing of our estimates will be set to 15 min as well.

Relative positioning was only carried out in loosely constrained kinematic mode (only for 3 mm/$\sqrt{h}$ approximately), because we will use this experiment for assessing the PPP ones. Since the clock is eliminated in the double differences, the interval between two consecutive estimates is 30 s, which corresponds to the sampling rate of the observations for this case. For the baseline configuration, we have chosen *txan* as the reference station as it is located in the center of the selected network, as can be seen in Figure 1. Pairs for differentiating only with respect to reference station have been included in the computations having baselines ranging from 56 to 353 km. Detailed distances can be seen in Table 1. Both for PPP and relative we have discarded observations below 7° over the horizon, and the weighting function of the observations has been considered as a negative exponential of the elevation angle of the transmitter.

All four experiments depicted in Table 2 have been analyzed in Appendix A; the methodology was validated by studying the repeatability of the sites coordinates, where it is known from previous studies that accounting for the gradients on GPS processing causes a better repeatability (see, e.g., Bar-Sever et al., 1998; MacMillan, 1995). Accordingly, it was observed that for all the receivers in our study, the repeatability improves about 25% when the gradients are estimated. Moreover, we have also tested the repeatability for different processing strategies and modes: absolute and relative positioning in static and in kinematic modes. We have found that the looser the constrains on the coordinates, then the more affected the coordinates are when neglecting the gradients. Moreover, relative positioning showed to be more sensitive to not

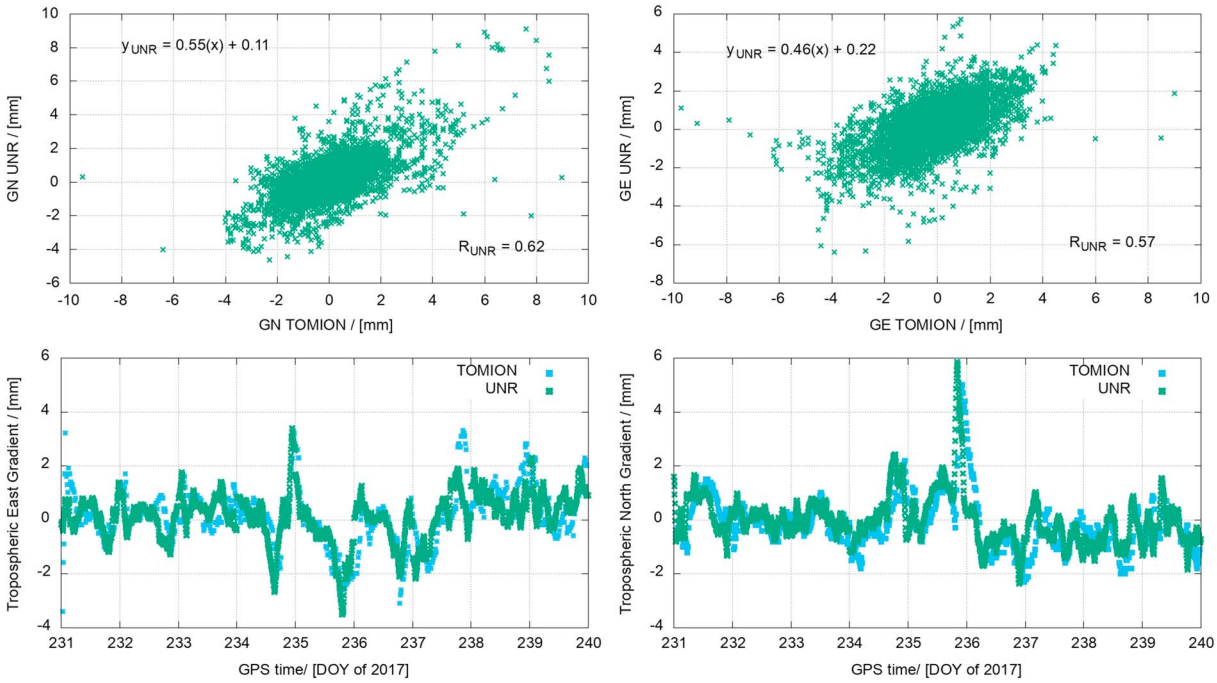

Figure 4. TOMION and UNR tropospheric east (left) and north (right) gradients for *sam2*. (top row) Correlation and coefficients in annotations at the bottom right. Linear regression at the top left. (bottom row) Time series from both sources. TOMION = TOmographic Model for precise IOnospheric sounding and GNSS Navigation; UNR = University of Nevada, Reno; DOY = day of year.

considering the gradients than absolute positioning. We have also seen that the horizontal gradients differed under 1 mm among all the procedures; hence, any set of gradients was valid for the study of the dynamics of the hurricane. With these statistics we were able to say that we can rely on our in-house software, since we have internally validated it obtaining consistent and comparable results with different modes and strategies.

2.4. Validation Versus UNR Products

For validating and comparing TOMION's estimates, UNR (University of Nevada, Reno, USA) products (Blewitt et al., 2018) have been downloaded from its server, which are provided with a 5-min sampling rate. Comparisons were performed for 10 of the 11 sites studied (*lcsm* was not available), and correlations coefficients of 0.57 and 0.62 were found for the east and north gradients, respectively. The linear regression performed between the TOMION and UNR east gradient time series resulted in 0.46 mm/mm for the slope and 0.22 mm for the independent term, while that for the north component resulted in 0.55 mm/mm and 0.11 mm. These results imply that there are no significant biases between the series.

The discrepancies found between the different sources can be explained by the fact that the external source applies flat weighting on the observations, while TOMION makes use of negative exponential of the elevation angle of the transmitter. Another cause of scale differences can be the different mapping functions used for the gradient term: Chen and Herring (1997) in TOMION and Bar-Sever et al. (1998) in GIPSY, and as it is stated in Kačmařík et al. (2018), systematic errors effects of up to 0.3 mm were observed in estimated tropospheric gradients when using different gradient mapping functions which depend on the applied observation elevation-dependent weighting as well. Furthermore, in TOMION, we use VMF1, whereas UNR adopts GMF (Global Mapping Function; Böhm et al., 2006) for mapping the symmetric term (m_d and m_w in equation (2)).

The temporal evolution of the two series can be seen in the bottom row in Figure 4, where one can appreciate that they are in in great coherence. Also, there is a slight time delay of TOMION's estimates with respect to the reference, which could be a reasonable explanation for the correlations coefficients estimated. The aspect that we want to remark here is that UNR gradients as long as TOMION's estimates are able to detect *anomalies*, which will be the focus of our study. For example, such gradients can be appreciated on *sam2* north parameter, almost at UTC midnight for DOY 236.

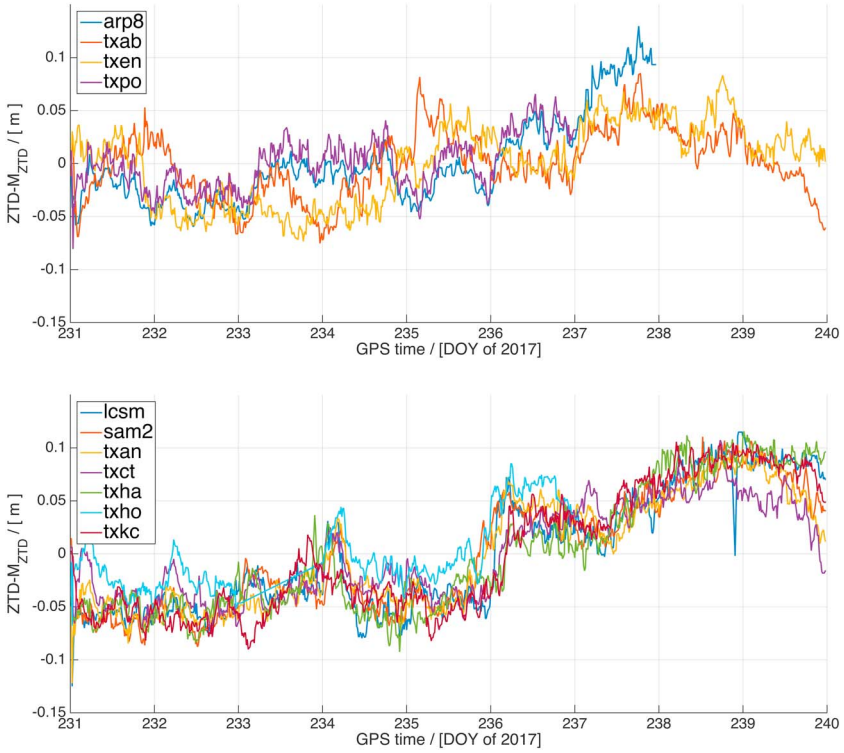

Figure 5. Time series of the *ZTD* for the 11 sites used for this experiment: (top) the sites on the coast and the ones further away; (bottom) the rest. For clarity of the plot, the mean of each series has been subtracted.

In this section we have introduced the software we are using for our computations, TOMION, and briefly explained the processing strategy. Then we have validated the estimations with an independent source (UNR) and with an independent strategy within the same software (relative positioning) which has been detailed in Appendix B. Even though there are some differences, the results and the estimated parameters show to be coherent between the different softwares or modes. Now we will proceed to analyze the behavior of the time series.

3. The Hurricane Harvey Test Case

3.1. ZTD

The *ZTD* is the main variable estimated with GPS that contains information of the lower atmosphere, and we have observed clear patterns on it evidencing the advance of the storm toward the area. The evolution of the *ZTD* over DOYs 231–239 for the 11 sites are plotted in Figure 5, where the relative variation of the *ZTD* shows an increase of about 10 to 15 cm over the 9-day time window. We have plotted in the top panel the *ZTD* for four sites, two on the coast and two further inland: *arp8*, *txpo*, *txen*, and *txha*. The bottom panel corresponds to the other seven sites. Such a distinction has been done because their behavior is slightly different: The sudden increase noticed over midnight of DOYs 235 to 236 is larger for the subset of the bottom panel than that of the top. This increment clearly reflects the effect of the hurricane. This behavior is due to the increase of the partial pressure of water vapor (Seco et al., 2009), which is closely related to the *ZWD* (Askne & Nordius, 1987). Decreasing surface pressure values, that is, in a cyclone, cause a smaller *ZHD* (Saastamoinen, 1972); hence, the increase on the *ZTD* is due to the increase on the water vapor partial pressure.

We have analyzed the nature of the *ZTD*, and we define the *Quiet* state to a set of data where the atmosphere was relatively calm within the analyzed window. The criterion to split the series was the time for which the detrended *ZTD* reached an absolute maximum. As it can be seen in Figure 6, this time label was found to be approximately DOY 235.27 for sam2. Therefore, Quiet state is before such time and *Stormy* is after sam2, within days 232 and 238 inclusive of 2017, that is from 19 to 26 August. In this figure, we have also added the east and north horizontal gradients, which will be studied in detail in the following section.

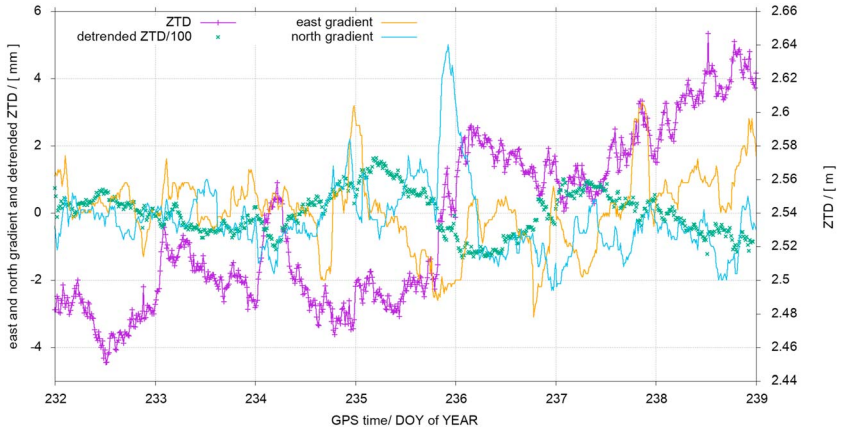

Figure 6. *ZTD* for *sam2* in DOYs of 2017, detrended *ZTD* (scaled by a factor of 100 to fit with the scale) and east and north gradients. The left *y* axis contains the values for $\tilde{Z}(t)$ and east and north gradients, and the right *y* axis for the *ZTD*.

We have considered a detrended *ZTD* (Hernández-Pajares et al., 2012) as

$$\tilde{Z} \equiv ZTD(t) - \frac{1}{2}\left[ZTD(t+\Delta t) + ZTD(t-\Delta t)\right] \tag{5}$$

where Δt was chosen as 24 hr, to mitigate effects of the local time, since we are subtracting from the *ZTD* value, the mean of the previous day and the following day. Each time tag found for each site, denoted as $\mathrm{DOY}_{\tilde{Z}_{MAX}}$, is depicted in Table 3 together with the maximum of *ZTD* series and its reference time, as well as the relative increment of the *ZTD* before and after $\mathrm{DOY}_{\tilde{Z}_{MAX}}$. The increase was found to be between 3.4% and 4.7% for 9 of the 11 sites. The other two, txen and *txab*, are the receivers located further away from the hurricane, which can be appreciated on the distance of the sites to the track of the hurricane. This increase in the mean of the *ZTD*, given by an increase on the *ZWD*, shows the heavy rains the area suffered after the hurricane struck land and weakened. In addition we have added the mean of the *ZTD* before and after $\mathrm{DOY}_{\tilde{Z}_{MAX}}$. It was also found that the maximum of the entire *ZTD* series of each station was found between 2 and 4 days after $\mathrm{DOY}_{\tilde{Z}_{MAX}}$, which shows that the water vapor actually accumulated after the hurricane hit Texas.

Table 3
Time Tag for the Maximum of the Directional Derivative of the ZTD

Site	$\mathrm{DOY}_{\tilde{Z}_{MAX}}$	$\overline{ZTD}_Q$	$\overline{ZTD}_S$	$\mathrm{DOY}_{ZTD_{MAX}}$	Max_{ZTD}	% of change	Distance to the track
arp8	235.948	2.579	2.650	237.760	2.726	4.0	114.501
txpo	235.833	2.580	2.670	237.802	2.743	3.5	115.3
txkc	235.260	2.527	2.645	238.885	2.678	4.7	255.608
txha	235.229	2.552	2.670	238.333	2.713	4.6	271.077
txct	235.302	2.526	2.611	238.729	2.663	3.4	329.044
lcsm	234.927	2.542	2.655	238.917	2.731	4.4	335.772
txan	235.438	2.473	2.571	238.594	2.611	4.0	350.016
txho	235.802	2.484	2.574	237.729	2.660	3.6	376.465
sam2	235.270	2.490	2.597	238.521	2.647	4.3	382.459
txen	233.760	2.375	2.441	238.760	2.485	2.8	576.211
txab	233.896	2.421	2.458	237.781	2.523	1.5	689.042

Note. Mean for the period with storm and without, ZTD's maximum and the relative change during the storm for the *ZTD*. Note that the table has been ordered with respect to the minimum distance to the track, which is expressed in the last column. Units in DOYs of 2017 and meters, except for distance to track which is in kilometers. ZTD = zenith tropospheric delay; DOY = day of year.

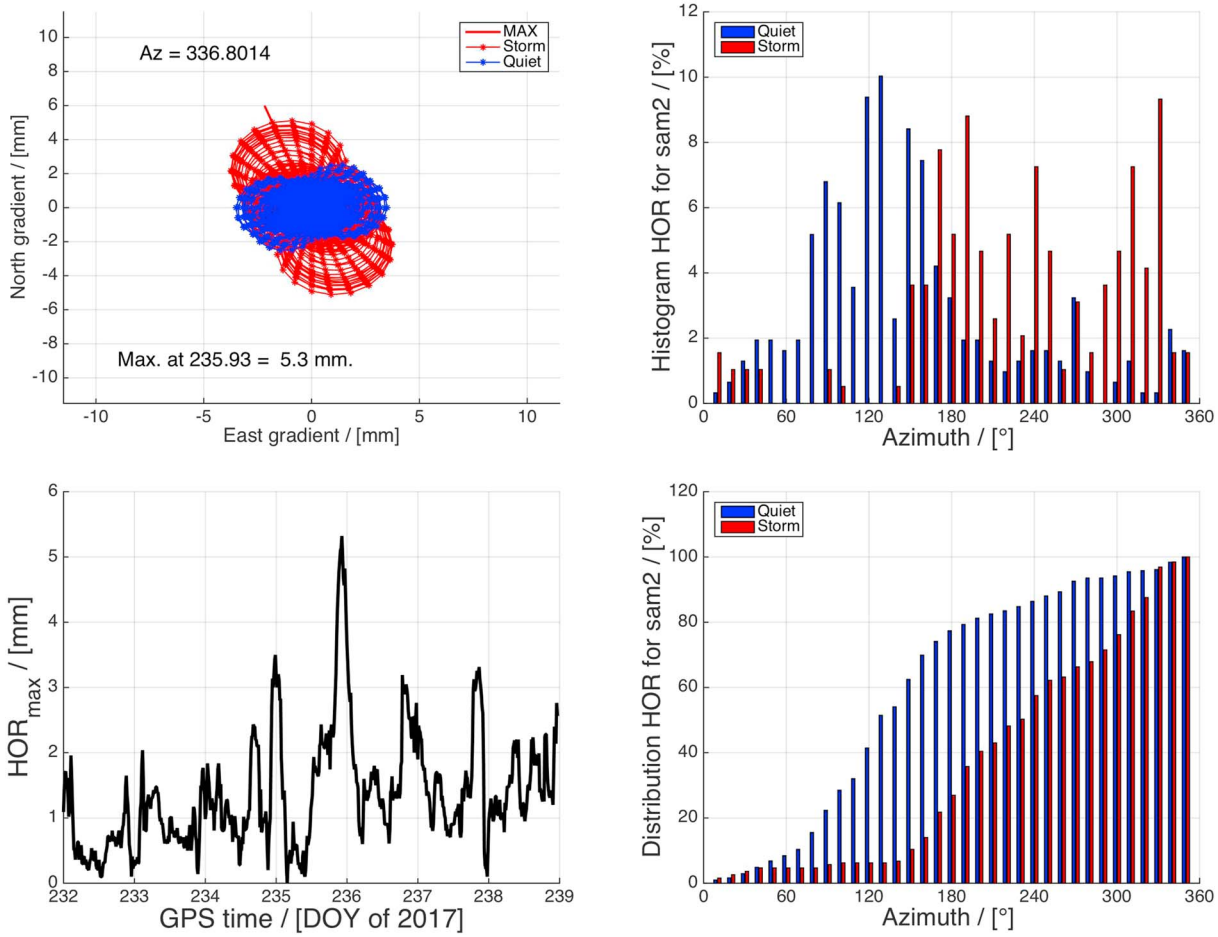

Figure 7. (top left) *HOR* as a function of azimuth and time, where one symmetric curve is plotted per epoch. (top right) Occurrence of azimuths for maximums of *HOR*. (bottom left) |*HOR*| as a time series. (bottom right) Probability distribution of azimuths of maximums of *HOR* for *sam2*.

3.2. Tropospheric Horizontal Gradients

The characteristics seen on the *ZTD* has driven this study to analyze the horizontal gradients associated with this phenomena, since it is expected that the atmosphere presents a strong asymmetry when the hurricane is close or over the area. Therefore, we have studied to what extent the GPS-estimated horizontal tropospheric gradients contain actual atmospheric information related to the front. As we mentioned before, the strategy chosen was PPP, in which the coordinates have been treated as a random walk process where the present epoch is related to the previous by 3 mm/$\sqrt{h}$. Hence, the gradients to be analyzed on the present section are estimated within such strategy. However, the gradients for the different processing strategies showed discrepancies of up to 0.1 mm.

Then, for each pair of G_N and G_E the correction has been computed for azimuths ranging from 0° to 360°, like the *ZTD* directional derivative

$$HOR(t,\alpha) = G_N(t)cos(\alpha) + G_E(t)sin(\alpha), \tag{6}$$

and the maximum *ZTD* directional derivative is equal to the gradient modulus, as $HOR_{\max} = (G_E^2 + G_N^2)^{1/2}$. At the top left panel of Figure 7, we are showing the time and azimuthal dependent correction to the zenith path delay, *HOR* as it is expressed by equation (6). The step taken for the plot was 10° in azimuth and 15 min in time, this last one given by the processing resolution interval. Therefore, we have one symmetric curve per each epoch, the orientation of which will depend on the signs of the coefficients G_N and G_E and its absolute value on the composition of the east and north components. Each *HOR* curve for a fixed time, $HOR(t_0)$, represents the correction to be performed for an individual epoch and for all azimuths. Furthermore, $HOR(t_0, \alpha_0)$ is the amount that such line of sight needs to be corrected for. This implies that large G_N

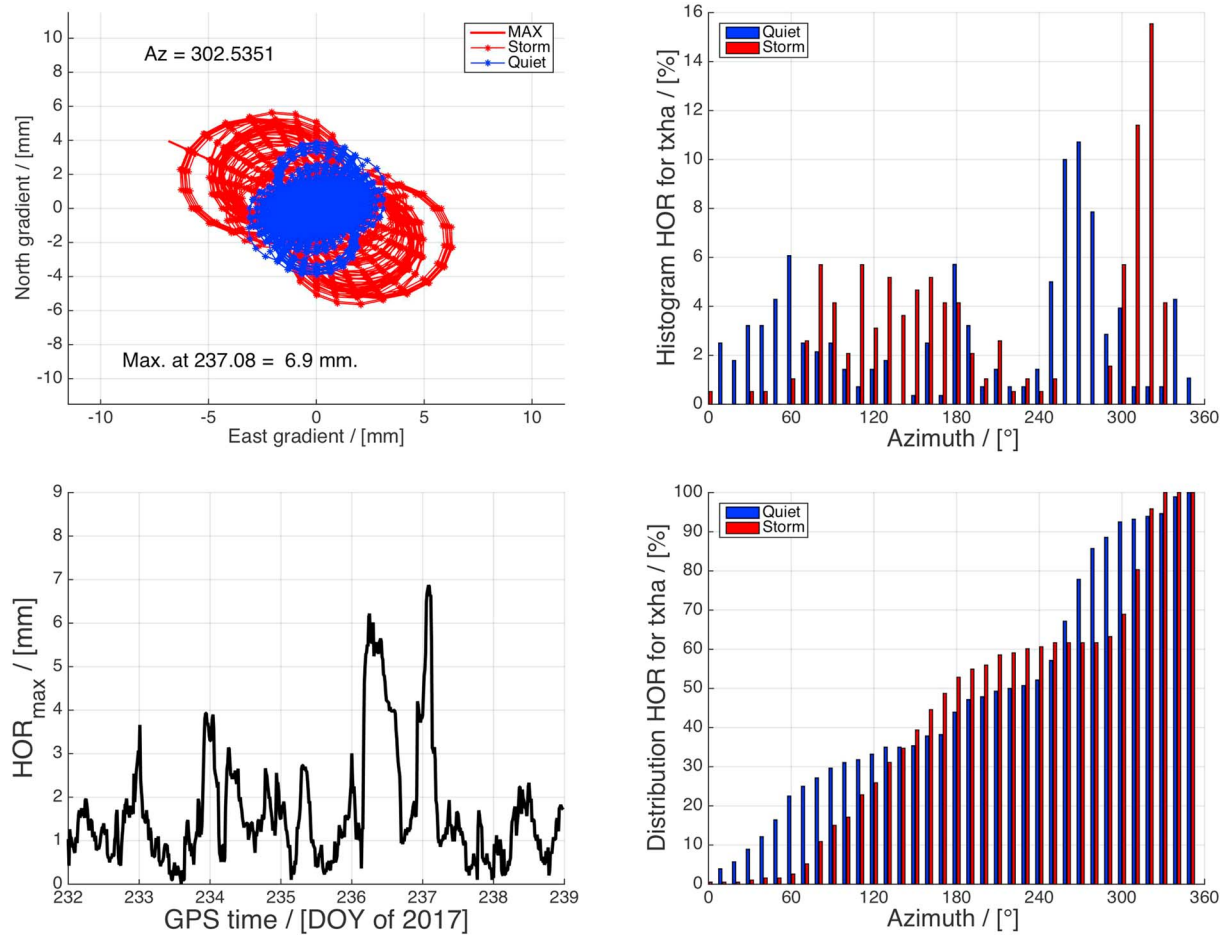

Figure 8. (top left) *HOR* as a function of azimuth and time, where one symmetric curve is plotted per epoch. (top right) Occurrence of azimuths for maximums of *HOR*. (bottom left) |*HOR*| as a time series. (bottom right) Probability distribution of azimuths of maximums of *HOR* for *txha*.

and G_E do not necessarily mean large *HOR*. The actual applied correction will depend on the position of the transmitter at time t_0. To study the behavior of this correction during the storm, we have represented *HOR* for *Storm* state in red, as defined by the detrended *ZTD* criteria, and for the Quiet period in blue. It is clear that from $\mathrm{DOY}_{\bar{Z}_{MAX}}$ onward, *HOR* departed from its nominal behavior in direction and modulus. The larger red line depicts the absolute maximum of the *HOR* series, which from now on it will be referred to as anomalous gradient, and its corresponding angle, time, and value are annotated over the top/bottom left of the figure.

On the top right panel of Figure 7, the histogram represents in percentage the occurrence of each azimuth from 0° to 360° for days categorized as Storm and for Quiet days, correspondingly in red and blue bars with a sampling of 10°. This means that for each pair G_N and G_E, the azimuth has been computed as

$$\alpha = \tan^{-1}\left(\frac{G_E}{G_N}\right). \tag{7}$$

We have also interpreted the occurrence of each azimuth as the normalized cumulative histogram, or cumulative distribution function, where, again, the Quiet state (blue bars) has a steeper slope for azimuths from 60° to 180°, while such increment for the Storm (red bars) state is after 180°.

Therefore, one can conclude that the preferred orientation when the atmosphere is not suffering an extreme event, according to the maximum detrended *ZTD* criteria, is rather toward southeast, as the blue bars do reflect, coincident with the Gulf of Mexico position. However, for those days when the hurricane made a pass through the studied region, we notice an opposite behavior: The maximum horizontal gradient directions point to the northwest. Again, this is for sam2 but will be extended for all sites. The bottom left panel in

Table 4
Horizontal Anomalous Gradient Magnitude, Its DOY of Occurrence, and the Mode of the Distributions for Quiet and Storm Periods

Site	G_N	G_E	HOR	$DOY_{HOR_{MAX}}$	$DOY_{\bar{Z}_{MAX}}$	Az_{MAX}	Az_Q	Az_S
arp8	−1.9	3.1	3.6	235.51	232.44	122	160	180
lcsm	2.4	4.0	4.7	235.01	235.20	59	280	130
sam2	4.9	−2.1	5.3	235.93	235.26	337	130	330
txab	4.5	−2.0	4.9	235.18	234.11	336	140	310
txan	4.2	−1.9	4.6	236.10	235.23	336	120	340
txct	3.1	−1.4	3.4	236.51	235.69	336	90	330
txen	0.7	−4.9	4.9	234.75	234.36	278	240	280
txha	3.7	−5.8	6.9	237.08	234.91	303	—	320
txho	3.9	−1.5	4.2	236.04	235.23	339	—	320
txkc	7.9	−3.4	8.6	236.38	235.23	337	—	290
txpo	−0.9	3.0	3.1	235.48	236.02	107	—	40

Note. Time tag for the maximum detrended *ZTD* of the *ZTD* has also been added. Units in millimeters, days, and degrees for gradients, DOYs, and angles, respectively. ZTD = zenith tropospheric delay; DOY = day of year.

Figure 7 comes to add information regarding the absolute value of the gradient vector, $HOR_{\max}$, with a clear maximum for epoch around 235.9, which is the magnitude of the anomalous gradient for sam2. Combining the four figures, where the particular case of sam2 is presented, it is clear that the Quiet behavior of the gradients are rather small vectors showing up to 3 mm, whose directions are mostly over the southeast, while for Stormy conditions the corrections are larger and up to 5 mm, where for this case its maximum is reached, and the preferred orientation is rather north northwest.

In Figure 8 we are showing the same plots as in Figure 7 now for the site txha. This site presents a change in orientation and in magnitude of its horizontal gradients before and after the time tag $DOY_{\bar{Z}_{MAX}}$, similarly to what has been detailed for sam2 above. The anomalous gradient for this site can be noticed at DOY 237.08, reaching a value of 6.9 mm. We have included these figures for txha to illustrate a case in which the histogram on the top right panel shows no preferent orientation of the horizontal gradients over the Quiet period. This characteristic over the Quiet period is seen also on txen, *txho*, *txkc*, and txpo and has been annotated as a dash (—) in Table 4. On the other hand, the distribution for the Storm period shows clear higher occurrence for the azimuths on the third quadrant. This behavior, shared among most sites, can also be appreciated on the cumulative histogram on the bottom right, where the percentage of horizontal gradients over the storm period rapidly increases after around 300–310°.

For 8 out of 11 sites we have found that the described behavior for sam2 or txha is replicated, as it is showed in Table 4, where the last two columns represent the center of the distribution for Quiet and Storm state, if any. This means that the Stormy time window showed centers of the distributions for the histograms clearly on the fourth quadrant mostly, that is, toward northwest, while for the Quiet period it was found rather on the second quadrant (like sam2) or with no preferent orientation at all (like txha). For assessing the previous for all sites, we have computed the azimuth, the absolute value and its components for each Stormy condition on the gradient time series like in Figure 7 bottom panel, and only accounting for one per site. Of course for each site, the time tag is different, because it is computed from its corresponding *ZTD* series. Furthermore, we have computed the distributions for the Quiet days and for four sites the histogram was rather planar, reflecting no typical orientation of its corrections (clarified as "—" in Table 4). The other seven sites showed azimuths for the Quiet period on the second quadrant, while for two of them it was on the same orientation than in the Stormy period. Only three of the sites, txen, arp8 and txpo, showed similar distribution for red and blue bars, two of which are located on the coast, probably suffering strong wet gradients due to the water vapor convection happening on a regular basis, whether a storm is approaching or not, where its corrections are rather on the second quadrant for all the days studied. Summarizing, 8 out of 11 sites present changes in orientation and magnitude during the approach of the hurricane.

The 850-hPa geopotential height and the corresponding wind vectors plotted in Figure 9, where the field values have been taken from Saha et al. (2011), contribute to the interpretation of the anomalies found on the

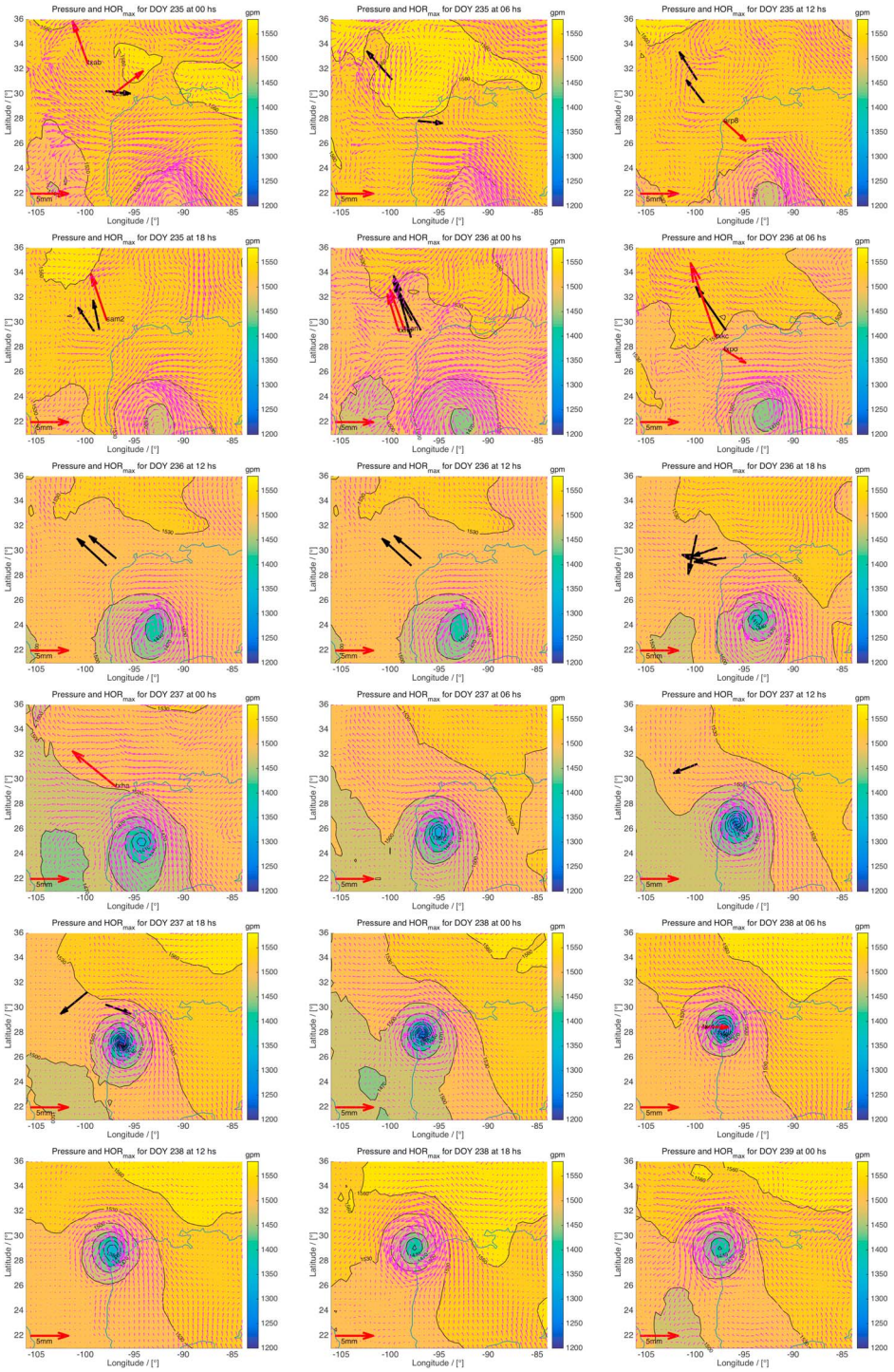

Figure 9. *Anomalous* gradient plotted as red arrows and maximum horizontal gradient detected on the given 6-hr time window, in black arrows. The geopotential height field clearly denotes the development of the hurricane. The maximum gradients appear perpendicular to the isobars and 1 to 3 days before the hurricane approached the area. The wind field in magenta is the wind field at 850 hPa. The red arrow at the bottom left corresponds to the scale of the GPS gradients.

horizontal tropospheric gradients. We have considered the 850-hPa isobaric level because its average altitude is 1,500 m, where the concentration of water vapor and the distribution of the air pressure is analogous to that of the surface, but where the wind fields are not affected by the friction with the surface. The sequence of plots represents the fields every 6 hr, starting on 23 August (DOY 235) at 00 hr and ending on 27 August (DOY 239) at 06 hr. From them, it is evident that the approach phase of the hurricane to the studied area is on 23 and 24 August, the highest intensity moments are on the 25th and early 26th, and the weakening phase rapidly after the landfall is on the 26th at 03 hr. The red arrows drawn on the figures are the anomalous horizontal gradients found above, and the black arrows correspond to the horizontal gradients found for the given time window for each site that are larger than 3 mm. All of them are located on the corresponding receiver (starting point of each arrow) and on 6-hr time windows. From this figure it is clear that the anomalous and large horizontal gradients appear in the stage prior to the placing of the hurricane over the studied area when the GPS signal is able to detect an asymmetry on the atmosphere. Noticeably, they point in the same direction than the horizontal pressure gradient, which is represented by the horizontal geopotential gradient of the 850-hPa isobaric surface. As it surges from the gradient wind relationship, the resulting wind would be perpendicular to the horizontal pressure gradient at that isobaric level and hence to the GPS anomalous gradients we have studied in this work. The maximum growth direction, given by these peaks, also denote the depression caused by the cyclone. These gradients are sensing the northern part of the system and evidencing the tilting angle of the troposphere as in Figure 3. When the hurricane is over the studied area (e.g. for Aug. 25th 00h onwards), then only one of the anomalous gradients occur (txct) and only three horizontal gradients larger than 3 mm are present. These latter are probably wet gradients, while those that occurred on the approach phase are likely hydrostatic gradients. The state of the atmosphere over the studied area at this point is rather symmetric; thus, the *ZTD* shows small horizontal gradients. We can also appreciate that most of the peaks happen from 1 to 3 days before the hurricane reached the area, which gives these parameters the use for studying and contributing to the potential warning of this type of events.

4. Conclusions

GPS Meteorology is a highly effective and robust technique to sense the atmosphere, providing continuous observations of atmospheric variables at almost no extra cost and with high spatiotemporal resolution. This research indicates that GPS-estimated tropospheric horizontal gradients have shown to be useful to study the stages prior to a hurricane arrival at an area. In this contribution, observation data from CORS network were processed and analyzed to retrieve tropospheric gradients for the time window and area where Hurricane Harvey struck land on 26 August 2017.

The estimation of the parameters has been performed with an in-house software that is well known for ionospheric determination; hence, we have included in this study the validation of the methodology as well as the validation of the parameters. We have seen in four different experiments that the coordinates repeatabilities improve when the tropospheric gradients are included on the processing as two additional unknowns, supporting the validity of the implemented methodology. The gradients themselves were validated with a databank from University of Reno, Nevada, where a great agreement was seen, showing correlations of above 50% for both east and north gradients.

We have analyzed the nature of the time-dependent parameter *ZTD* over the DOYs 231 through 240 of year 2017, where Hurricane Harvey approached and reached Texas, USA, on DOYs 234–236. We have seen that the *ZTD* experienced an increase of from 3.4% to 4.7% for 9 of the 11 sites. The other two are located further away from the hurricane. This effect is closely related to the heavy rains that affected the area. For assessing the behavior of the horizontal tropospheric gradients, we have introduced a simple method for studying their direction and intensity during the approach of the hurricane. First, we have computed the moment for which the *ZTD* presented an absolute maximum of an approximation of its detrended *ZTD*. This procedure depicts a detrended *ZTD*, where the collection of all the largest inflection points allowed us to divide the series into Quiet and Storm periods, before and after such time tags, respectively. We have found that the distribution of the orientation of the horizontal gradients for the Storm period changes drastically from southeast to northwest, in general. Nominal behavior was noted as pointing to the Gulf of Mexico or with no preferent orientations. We have also observed that the extreme behavior of the gradients developed between 1 and 3 days before the hurricane made landfall, and they mostly appear orthogonal to the pressure isolines.

These findings indicate that GPS-estimated horizontal gradients can represent the passage and development of a severe weather event, and hence it can be used for studying and detecting them potentially in advance.

Appendix A: TOMION's Coordinates Estimation and Its Validation

Incorporating horizontal gradients in the estimation of coordinates in space geodetic techniques is well known to improve its repeatability (Bar-Sever et al., 1998; MacMillan, 1995). Since TOMION is well known for ionospheric determination, we will assess its reliability and that of our methodology, in terms of the repeatability of coordinates.

We have estimated the local coordinates for each site of the selected network for the four chosen strategies, for two case scenarios: Hurricane Harvey (DOYS 231–239) and a 10-day run (DOYS 51–59) for February of the same year, 2017, where the atmosphere was relatively calm. In both cases, a previous processing was performed to obtain an a priori set of coordinates for DOY 231 and DOY 51, respectively, and the statistics have been performed with respect to those final values. In Figure A1 we are showing horizontal repeatability for the all the receivers of the network for static PPP, tight kinematic PPP, loose kinematic PPP, and loose kinematic relative precise positioning, when the horizontal gradients are considered and when they are not. We can appreciate that in all cases, the horizontal repeatability improves when the horizontal gradients are included in the processing. Moreover, for the 51–59 run, the root-mean-squares (RMSs) are, in general, smaller than those for the 231–239 run, which is also reasonable due to the extremely different weather conditions.

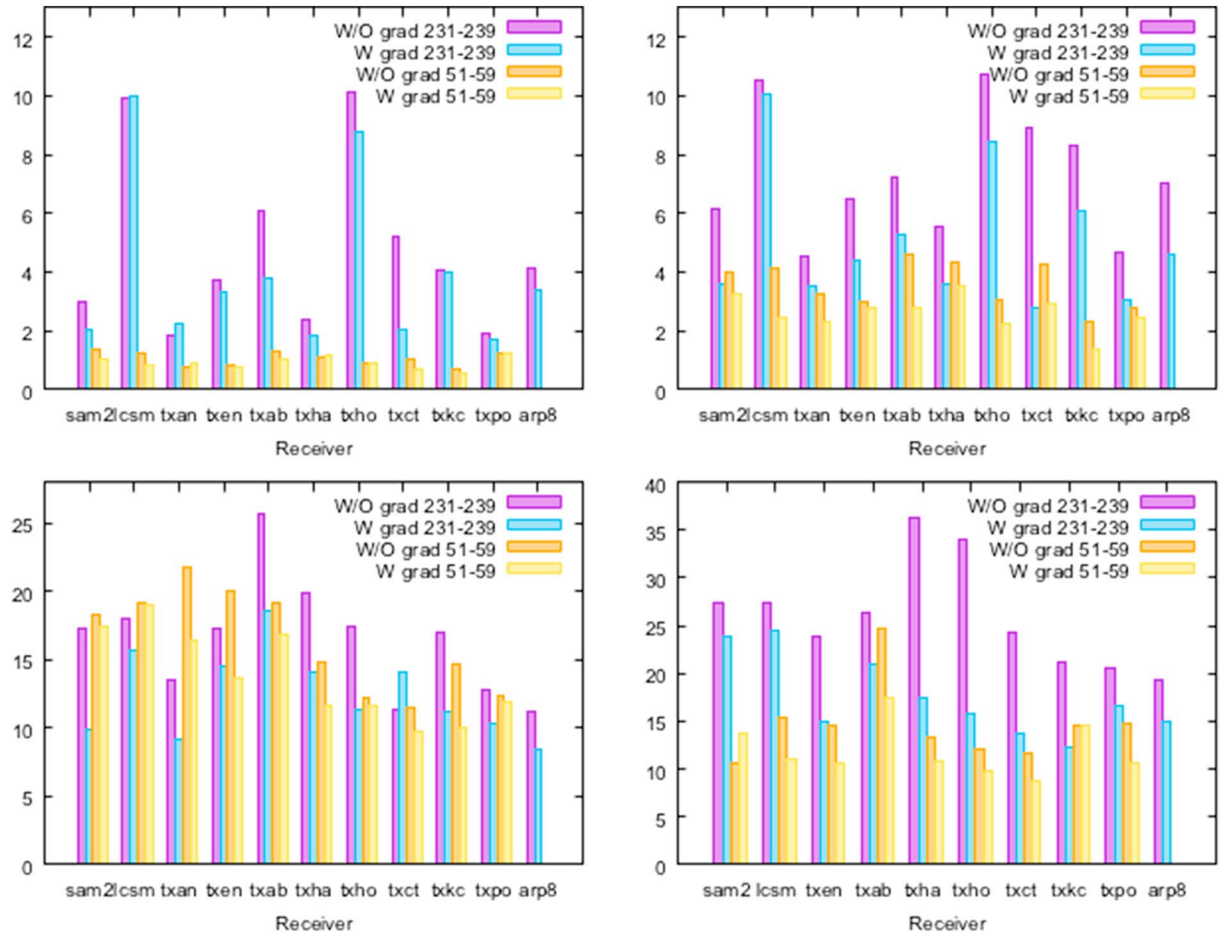

Figure A1. Horizontal coordinate repeatability when the tropospheric gradients are estimated (blue) and when they are not (purple) for PPP static solution (top left), for kinematic mode tightly constrained (top right), for kinematic loosely constrained (bottom left), and for relative mode loosely constrained (bottom right). All units are in millimeters. Data for *arp8* were not available for the winter period, and the site has been decommissioned. PPP = Precise Point Positioning.

Table A1
Relative Bias, SD, and RMS of the Coordinates for the Different Processing Modes for All the Stations

		Metric Γ			Metric Λ		
Period	Strategy	Γ_{Bias}	Γ_{SD}	Γ_{RMS}	Λ_{Bias}	Λ_{SD}	Λ_{RMS}
231–239	PPP Static	0.87	0.88	0.87	0.88	0.88	0.88
231–239	PPP Const.	0.74	0.76	0.75	0.72	0.69	0.72
231–239	PPP Loose	0.71	0.72	0.72	0.73	0.71	0.73
231–239	Relative	0.65	0.74	0.68	0.70	0.70	0.70
51–59	PPP Static	0.88	0.89	0.89	0.89	0.94	0.90
51–59	PPP Const.	0.75	0.65	0.73	0.75	0.69	0.73
51–59	PPP Loose	0.84	0.88	0.84	0.84	0.88	0.85
51–59	Relative	0.66	0.81	0.68	0.73	0.81	0.74

Note. First four rows correspond to the Hurricane Harvey DOYS, and the four last rows to a quiet period during the winter of the same year 2017. SD = standard deviation; RMS = root-mean-square; PPP = Precise Point Positioning.

We have chosen simple statistical measures to evaluate how each processing mode is affected by the estimations of gradients. In the first place, we have considered the mean of the ratios R of the biases of the coordinates with and without gradients with respect to an priori coordinate, computed with and without gradients, respectively. This metric is represented by the definition at Λ, while Γ is given by the ratio of the means of the biases (b) for each methodology, that is, considering and not considering the gradients:

$$\Lambda = \frac{1}{N}\sum_{i}^{N} R_i \qquad \text{and} \qquad \Gamma = \frac{\frac{1}{N}\sum_{i}^{N} b_i^{\text{grad}}}{\frac{1}{N}\sum_{i}^{N} b_i^{\text{nograd}}}, \tag{A1}$$

where N is the number of sites, 11 in this case. For the RMS and the SD (standard deviation), the analogous procedure has been performed. These metrics have been computed for all of the sites and are depicted in the first four rows of Table A1. For both metrics, and for all processing modes, the position accuracy will be degraded by from 12% to 35% if horizontal symmetry of the atmosphere is assumed, in the presence of a weather front, for the period of the hurricane and from 6% to 34% for the winter period, considering their bias, SD, or RMS with respect to an a priori coordinate. We can also appreciate in the last four rows of the same table that, for the analysis during the winter, the implications of not considering the gradients is slightly less important than when strong meteorological forcing occurs.

The differences between gradients computed for the different processing modes are under the statistical error of the estimations. This means that the different setups chosen for the coordinates do not have a significant impact on the horizontal gradients. We have chosen the gradients computed on the loosely constrained mode for the coordinates to analyze if they represent the behavior of the atmosphere during the hurricane.

Hence, we have been able to reproduce established results regarding the stability of the site's coordinates, for most of the cases in all the setups proposed. The WARTK methodology, widely validated, presents results analogous to that of PPP; therefore, we can conclude that our results are consistent. Also, we have shown that neglecting the gradients has more impact the looser the kinematic processing is, and slightly even more for relative mode. The reason why differentiating the observables can show to have more impact on the stability of the processing can be the baselines aligned with the front accumulating more asymmetric delay than those orienting perpendicular to it (Ichikawa et al., 1995).

Appendix B: TOMION's Horizontal Gradient Intra-Software Validation

Figure B1 shows the coherence between TOMION horizontal gradients for absolute and relative processing mode, both for kinematic in its loosely constrained setup. For each epoch where the estimation of the north and east tropospheric gradients were available for both processing modes, which is every 15 min, the horizontal absolute value of the gradients was computed, as the square root of the addition of the squared components, and a correlation of 62% was obtained for the time series.

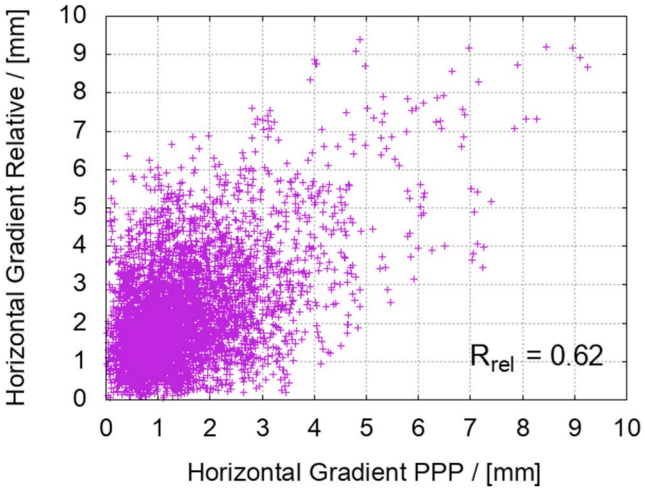

Figure B1. Correlation between magnitude of TOMION horizontal gradients in relative and in absolute mode for kinematic processing, with process noise equal to 3 mm/$\sqrt{h}$. Correlation coefficient annotated at the bottom right, denoted as R_{rel}. TOMION = TOmographic Model for precise IOnospheric sounding and GNSS Navigation; PPP = Precise Point Positioning.

Acknowledgments
The GPS observations for this work have been downloaded from cddis.gsfc.nasa.gov, and the wind fields and the geopotential heights have been obtained from ncar.ucar.edu. The authors kindly appreciate the availability of the data.

References

Askne, J., & Nordius, H. (1987). Estimation of tropospheric delay for microwaves from surface weather data. *Radio Science*, *22*(3), 379–386. https://doi.org/10.1029/RS022i003p00379

Bar-Sever, Y. E., Kroger, P. M., & Borjesson, J. A. (1998). Estimating horizontal gradients of tropospheric path delay with a single GPS receiver. *Journal of Geophysical Research*, *103*(B3), 5019–5035. https://doi.org/10.1029/97JB03534

Bevis, M., Businger, S., Herring, T. A., Rocken, C., Anthes, R. A., & Ware, R. H. (1992). GPS meteorology: Remote sensing of atmospheric water vapor using the Global Positioning System. *Journal of Geophysical Research*, *97*(D14), 15,787–15,801. https://doi.org/10.1029/92JD01517

Blewitt, G., Hammond, W., & Kreemer, C. (2018). Harnessing the GPS data explosion for interdisciplinary science. *Eos*, *99*. https://doi.org/10.1029/2018EO104623

Böhm, J., Niell, A., Tregoning, P., & Schuh, H. (2006). Global Mapping Function (GMF): A new empirical mapping function based on numerical weather model data. *Geophysical Research Letters*, *33*, L07304. https://doi.org/10.1029/2005GL025546

Böhm, J., & Schuh, H. (2004). Vienna mapping functions in VLBI analyses. *Geophysical Research Letters*, *31*, L01603. https://doi.org/10.1029/2003GL018984

Boniface, K., Ducrocq, V., Jaubert, G., Yan, X., Brousseau, P., Masson, F., et al. (2009). Impact of high-resolution data assimilation of GPS zenith delay on Mediterranean heavy rainfall forecasting. *Annales Geophysicae*, *27*, 2739–2753. https://doi.org/10.5194/angeo-27-2739-2009

Brunini, C. (2007). Sirgas: Sistema de referencia geocéntrico para las Américas, La Plata, Argentina Simposio "IDE América: Conceptos, Prácticas y Proyectos.

Bruyninx, C., Habrich, H., Söhne, W., Kenyeres, A., Stangl, G., & Völksen, C. (2012). Enhancement of the EUREF permanent network services and products, *Geodesy for Planet Earth* (pp. 27–34). Switzerland: Springer. https://doi.org/10.1007/978-3-642-20338-1_4

Chen, G., & Herring, T. (1997). Effects of atmospheric azimuthal asymmetry on the analysis of space geodetic data. *Journal of Geophysical Research*, *102*(B9), 20,489–20,502. https://doi.org/10.1029/97JB01739

Dach, R., Lutz, S., Walser, P., & Fridez, P. (2015). Bernese GNSS software version 5.2.

Davis, J., Herring, T., Shapiro, I., Rogers, A., & Elgered, G. (1985). Geodesy by radio interferometry: Effects of atmospheric modeling errors on estimates of baseline length. *Radio Science*, *20*(6), 1593–1607. https://doi.org/10.1029/RS020i006p01593

De Haan, S. (2013). Assimilation of GNSS ZTD and radar radial velocity for the benefit of very-short-range regional weather forecasts. *Quarterly Journal of the Royal Meteorological Society*, *139*(677), 2097–2107. https://doi.org/10.1002/qj.2087

Dousa, J., & Vaclavovic, P. (2014). Real-time zenith tropospheric delays in support of numerical weather prediction applications. *Advances in Space Research*, *53*(9), 1347–1358. https://doi.org/10.5194/amt-10-3589-2017

Dousa, J., Vaclavovic, P., & Elias, M. (2017). Tropospheric products of the second GOP European GNSS reprocessing (1996–2014). *Atmospheric Measurement Techniques*, *10*(9), 3589–3607.

Elgered, G., Ning, T., Forkman, P., & Haas, R. (2018). On the information content in linear horizontal delay gradients estimated from space geodesy observations. *Atmospheric Measurement Techniques Discussions*, *2018*, 1–24. https://doi.org/10.5194/amt-2018-318

GGOS (2017). Global Geodetic Observing System, http://ggosatm.hg.tuwien.ac.at/

Guerova, G., Jones, J., Douša, J., Dick, G., Haan, S. d., Pottiaux, E., et al. (2016). Review of the state of the art and future prospects of the ground-based GNSS meteorology in Europe. *Atmospheric Measurement Techniques*, *9*(11), 5385–5406. https://doi.org/10.1007/978-3-642-10634-7_86

Hernández Pajares, M., Juan, J. M., Sanz, J., Aragón-Ángel, A., Ramos-Bosch, P., Samson, J., et al. (2010). Wide-area RTK: High precision positioning on a continental scale. *Inside GNSS*, *5*(2), 35–46.

Hernández-Pajares, M., Juan, J., Sanz, J., & Aragón-Àngel, A. (2012). Propagation of medium scale traveling ionospheric disturbances at different latitudes and solar cycle conditions. *Radio Science*, *47*, RS0K05. https://doi.org/10.1029/2011RS004951

Hernández-Pajares, M., Juan, J., Sanz, J., & Colombo, O. (2002). Improving the real-time ionospheric determination from GPS sites at very long distances over the equator. *Journal of Geophysical Research*, *107*(A10), 1296. https://doi.org/10.1029/2001JA009203

Hernández-Pajares, M., Juan, J. M., Sanz, J., Colombo, O. L., & van der Marel, H. (2001). A new strategy for real-time integrated water vapor determination in WADGPS networks. *Geophysical Research Letters*, *28*(17), 3267–3270. https://doi.org/10.1029/2001GL012930

Hernández-Pajares, M., Zomoza, J., Subirana, J. S., & Colombo, O. L. (2003). Feasibility of wide-area subdecimeter navigation with Galileo and modernized GPS. *IEEE Transactions on Geoscience and Remote Sensing*, *41*(9), 2128–2131. https://doi.org/10.1109/TGRS.2003.817209

Herring, T., King, R., & McClusky, S. (2006). Gamit reference manual. *GPS Analysis at MIT, Release*, *10*, 36.

Kačmařík, M., Douša, J., Dick, G., Zus, F., Brenot, H., Möller, G., et al. (2017). Inter-technique validation of tropospheric slant total delays. *Atmospheric Measurement Techniques*, *10*(6), 2183–2208.

Kačmařík, M., Douša, J., Zus, F., Václavovic, P., Balidakis, K., Dick, G., & Wickert, J. (2018). Sensitivity of GNSS tropospheric gradients to processing options. In *Annales Geophysicae* (Vol. 3, No. 3, pp. 429–446). Copernicus GmbH.

Karabatić, A., Weber, R., & Haiden, T. (2011). Near real-time estimation of tropospheric water vapour content from ground based GNSS data and its potential contribution to weather now-casting in Austria. *Advances in Space Research*, *47*(10), 1691–1703. https://doi.org/10.1016/j.asr.2010.10.028

Li, X., Zus, F., Lu, C., Ning, T., Dick, G., Ge, M., et al. (2015). Retrieving high-resolution tropospheric gradients from multiconstellation GNSS observations. *Geophysical Research Letters*, *42*, 4173–4181. https://doi.org/10.1002/2015GL063856

Lu, C., Li, X., Li, Z., Heinkelmann, R., Nilsson, T., Dick, G., et al. (2016). Gnss tropospheric gradients with high temporal resolution and their effect on precise positioning. *Journal of Geophysical Research: Atmospheres*, *121*, 912–930. https://doi.org/10.1002/2015JD024255

MacMillan, D. (1995). Atmospheric gradients from very long baseline interferometry observations. *Geophysical Research Letters*, *22*(9), 1041–1044. https://doi.org/10.1029/95GL00887

Marini, J. W. (1972). Correction of satellite tracking data for an arbitrary tropospheric profile. *Radio Science*, *7*(2), 223–231. https://doi.org/10.1029/RS007i002p00223

Meindl, M., Schaer, S., Hugentobler, U., & Beutler, G. (2004). Tropospheric gradient estimation at CODE: Results from global solutions. *Journal of the Meteorological Society of Japan Series II*, *82*(1B), 331–338. https://doi.org/10.2151/jmsj.2004.331

Milliner, C., Materna, K., Bürgmann, R., Fu, Y., Moore, A. W., Bekaert, D., et al. (2018). Tracking the weight of Hurricane Harvey's stormwater using GPS data. *Science Advances*, *4*(9), eaau2477.

Miyazaki, S., Iwabuchi, T., Heki, K., & Naito, I. (2003). An impact of estimating tropospheric delay gradients on precise positioning in the summer using the Japanese nationwide GPS array. *Journal of Geophysical Research*, *108*(B7), 2335. https://doi.org/10.1029/2000JB000113

Morel, L., Pottiaux, E., Durand, F., Fund, F., Boniface, K., de Oliveira Junior, P. S., & Van Baelen, J. (2015). Validity and behaviour of tropospheric gradients estimated by GPS in Corsica. *Advances in Space Research*, *55*(1), 135–149. https://doi.org/10.1016/j.asr.2014.10.004

Pacione, R., & Di Tomaso, S. (2016). A reference GNSS tropospheric dataset over Europe, *EGU General Assembly Conference Abstracts* (Vol. 18, pp. 12828). https://doi.org/10.5194/amt-10-1689-2017

Poli, P., Moll, P., Rabier, F., Desroziers, G., Chapnik, B., Berre, L., et al. (2007). Forecast impact studies of zenith total delay data from European near real-time GPS stations in météo france 4dvar. *Journal of Geophysical Research*, *112*, D06114. https://doi.org/10.1029/2006JD007430

Roma-Dollase, D., Hernández-Pajares, M., Krankowski, A., Kotulak, K., Ghoddousi-Fard, R., Yuan, Y., et al. (2017). Consistency of seven different GNSS global ionospheric mapping techniques during one solar cycle. *Journal of Geodesy*, *92*, 691–706. https://doi.org/10.1007/s0019

Saastamoinen, J. (1972). Atmospheric correction for the troposphere and stratosphere in radio ranging satellites, *The use of artificial satellites for geodesy* (vol. 15, pp. 247–251). Washington, DC: American Geophysical Union.

Sagiya, T. (2004). A decade of GEONET: 1994–2003. *Earth, Planets and Space*, *56*(8), xxix–xli. https://doi.org/10.1186/BF03353077

Saha, S., Moorthi, S., Wu, X., Wang, J., Nadiga, S., Tripp, P., et al. (2011). NCEP Climate Forecast System Version 2 (CFSV2) 6-hourly products. Boulder, CO: Research Data Archive at the National Center for Atmospheric Research, Computational and Information Systems Laboratory. https://doi.org/10.5065/D61C1TXF

Seco, A., González, P., Ramírez, F., García, R., Prieto, E., Yagüe, C., & Fernández, J. (2009). GPS monitoring of the tropical storm delta along the Canary Islands track, november 28-29, 2005. *Pure and Applied Geophysics*, *166*(8-9), 1519–1531.

Shoji, Y. (2013). Retrieval of water vapor inhomogeneity using the Japanese nationwide GPS array and its potential for prediction of convective precipitation. *Journal of the Meteorological Society of Japan Series II*, *91*(1), 43–62. https://doi.org/10.2151/jmsj.2013-103

Shoji, Y., Nakamura, H., Iwabuchi, T., Aonashi, K., Seko, H., Mishima, K., et al. (2004). Tsukuba GPS dense net campaign observation: Improvement in GPS analysis of slant path delay by stacking one-way postfit phase residuals. *Journal of the Meteorological Society of Japan Series II*, *82*(1B), 301–314. https://doi.org/10.2151/jmsj.2004.301

Thayer, G. D. (1974). An improved equation for the radio refractive index of air. *Radio Science*, *9*(10), 803–807. https://doi.org/10.1029/RS009i010p00803

Zhang, K., Manning, T., Wu, S., Rohm, W., Silcock, D., & Choy, S. (2015). Capturing the signature of severe weather events in Australia using GPS measurements. *IEEE Journal of Selected Topics in Applied Earth Observations and Remote Sensing*, *8*(4), 1839–1847. https://doi.org/10.1109/JSTARS.2015.2406313

Zumberge, J., Heflin, M., Jefferson, D., Watkins, M., & Webb, F. H. (1997). Precise point positioning for the efficient and robust analysis of GPS data from large networks. *Journal of Geophysical Research*, *102*(B3), 5005–5017. https://doi.org/10.1029/96JB03860

Zus, F., Douša, J., Kačmařík, M., Václavovic, P., Dick, G., & Wickert, J. (2019). Estimating the impact of global navigation satellite system horizontal delay gradients in variational data assimilation. *Remote Sensing*, *11*(1), 41. https://doi.org/10.3390/rs11010041